Enhanced pore space analysis by use of μ-CT, MIP, NMR, and SIP

Zeyu Zhang [1], Sabine Kruschwitz [2, 3], Andreas Weller [4], Matthias Halisch [5]

[1] Southwest Petroleum University, School of Geoscience and Technology, 610500 Chengdu, China
[2] Federal Institute for Material Research and Testing (BAM), D-12205 Berlin, Germany
[3] Technische Universität Berlin, Institute of Civil Engineering, D-13355 Berlin, Germany
[4] Clausthal University of Technology, Institute of Geophysics, D-38678 Clausthal-Zellerfeld, Germany
[5] Leibniz Institute for Applied Geophysics (LIAG), D-30655 Hannover, Germany

Correspondence to: Zeyu Zhang (zeyuzhangchina@163.com)

Abstract

We investigate the pore space of rock samples with respect to different petrophysical parameters using various methods, which provide data upon pore size distributions, including micro computed tomography (μ-CT), mercury intrusion porosimetry (MIP), nuclear magnetic resonance (NMR), and spectral induced polarization (SIP). The resulting cumulative distributions of pore volume as a function of pore size are compared. Considering that the methods differ with regard to their limits of resolution, a multiple length scale characterization of the pore space is proposed, that is based on a combination of the results from all of these methods. The approach is demonstrated using samples of Bentheimer and Röttbacher sandstone. Additionally, we compare the potential of SIP to provide a pore size distribution with other commonly used methods (MIP, NMR). The limits of resolution of SIP depend on the usable frequency range (between 0.002 Hz and 100 Hz). The methods with similar resolution show a similar behavior of the cumulative pore volume distribution in the overlapping pore size range. We assume that μ-CT and NMR provide the pore body size while MIP and SIP characterize the pore throat size. Our study shows that a good agreement between the pore radii distributions can only be achieved if the curves are adjusted considering the resolution and pore volume in the relevant range of pore radii. The MIP curve with the widest range in resolution should be used as reference.

Keywords: Pore Space Analysis, Joint Methods, Fractal Dimension, Spectral Induced Polarization

1 Introduction

Transport and storage properties of reservoir rocks are determined by the size and arrangement of the pores. In this paper we use the term geometry to refer to the relevant pore sizes, such as the pore throat radius, pore body radius, body to throat ratio, shape of the pore, and pore volume corresponding to certain pore radius. Different methods have been developed to determine the pore size distribution of rocks. These methods are based on different physical principles. Therefore, it can be expected that the methods recognize different geometries and sizes. Additionally, the ranges of pore sizes that are resolved by the methods are different (Meyer et al., 1997). Rouquerol et al. (1994) reported that no experimental method provides the absolute value of parameters such as porosity, pore size, surface area, and surface roughness.

An enhanced pore space analysis using different methods should be able to provide a better description of the pore space over a wide range of pore sizes. Our study of pore space analysis is based on the following methods: micro computed tomography (μ-CT), mercury intrusion porosimetry (MIP), nuclear magnetic resonance (NMR), and spectral induced polarization (SIP). The first three methods can be regarded as standard methods to derive a pore size distribution. Since these methods can reveal the inner structure of the rocks, they are widely applied in geosciences (e.g. Halisch et al., 2016b, Mees et al., 2003, Behroozmand et al., 2015, Weller et al., 2015). The main aim of our paper is to integrate an electrical method in this study. Electrical conductivity and polarizability (or real and imaginary part of electrical conductivity) are fundamental physical properties of porous materials. The SIP method measures the low-frequency electric behavior of rocks and soil material that can be efficiently represented by a complex electric conductivity. The electric properties of a porous material depend to a large extent on key parameters including the porosity, the grain and pore size distribution, the specific internal surface, the tortuosity, the saturation and the chemical composition of the pore-filling fluids. SIP is a non-destructive method that can be applied to characterize the geometry of the pore system. The use of SIP in this field has been reported only recently (Revil et al., 2014; Zhang et al., 2017).

We are aware that further methods can be applied for the characterization of pore size distribution, e.g. synchrotron-radiation-based computed tomography (Peth et al., 2008), focused ion beam tomography (Keller et al., 2011), transmission electron microscopy (Gaboreau et al., 2012), scanning electron microscopy (SEM), ^{14}C labeled methylmethacrylate method (Kelokaski et al., 2005), and gas adsorption and desorption method (BET) (Avnir and Jaroniec, 1989). Our study presents an approach to describe and quantify the pore space of porous material by combining the results of methods with different resolution. Samples of Bentheimer and Röttbacher sandstone are investigated by µ-CT, MIP, NMR, and SIP. The resulting pore size distributions are compared to each other to get two different pore radii distributions, one for the pore body radius and one for the pore throat radius. The comparison of the two curves enables the determination of the ratio between pore body and pore throat radius. Finally, the fractal dimension of the pore volume distribution is determined for the two samples. The fractal dimension is a useful parameter for up-and downscaling of geometrical quantities. Zhang and Weller (2014) investigated the fractal behavior of the pore volume distribution by capillary pressure curves and NMR T_2 distributions of sandstones. Considering the differences in fractal dimension resulting from the two methods, they concluded a differentiation into surface dimension and volume dimension. Additionally, the fractal dimension is used in methods of permeability prediction (e.g. Pape et al., 2009).

2 Theory

The pore size distribution resulting from different methods has to be compared and evaluated. We prefer a comparison based on the cumulative volume fraction of pores V_c, which is expressed by

$$V_c = \frac{V(<r)}{V_p}, \qquad (1)$$

with V_p being the total pore volume, and $V(<r)$ the cumulative volume of pores with radii less than r. A graph displaying the logarithm of V_c versus the logarithm of the pore radius offers the advantage that the slope of the curves is related to the fractal dimension of the pore volume (Zhang and Weller, 2014).

Fractal theory is applied to describe the structure of geometric objects (Mandelbrot, 1977, 1983). At molecular size and microscopic range, surfaces of most materials including those of natural rocks show irregularities and defects that appear to be self-similar upon variation of resolution (Avnir et. al, 1984). A self-similar object is characterized by similar structures at different scales. The regularity of self-similar structures can be quantified by the parameter of fractal dimension D. Pape et al. (1982) first proposed a fractal model (the so called ‘pigeon-hole model’ or ‘Clausthal Concept’) for the geometry of rock pores. Fractal dimension describes the size of geometric objects as a function of resolution. This parameter has proved to be useful in the comparison of different methods that determine distributions of pores in sandstones and carbonates (e.g. Zhang and Weller, 2014, Ding et al., 2017).

From MIP, the entry sizes of pores and cavities, which is referred to as pore throat radius r_t, can be determined according to the Washburn-equation (Washburn, 1921)

$$r_t = -\frac{2 \cdot \gamma \cdot \cos\theta}{P_c}, \quad (2)$$

with $\gamma = 0.48$ N/m being the surface tension of mercury, $\theta = 140°$ the contact angle between mercury and the solid minerals, and P_c the pressure of the liquid mercury that is referred to as capillary pressure.

The cumulative volume of mercury V_{Hg} corresponds to the pore volume $V(>r_t)$. It should be noted that the volume of larger pores, which are shielded by narrower throats, is attributed to the pore throat radius (e.g. Kruschwitz et al., 2016). Knowing the total pore volume V_p, the saturation of the sample with mercury S_{Hg} can be determined. A conventional capillary pressure curve displays the relationship between the saturation of the sample with mercury S_{Hg} as a function of capillary pressure P_c (e.g. Thomeer, 1960). Using the following simple transformations

$$S_{Hg} = \frac{V_{Hg}}{V_p} = \frac{V(>r_t)}{V_p} = \frac{V_p - V(<r_t)}{V_p} = 1 - V_c, \quad (3)$$

the cumulative volume fraction of pores V_c as defined in Eq. (1) can be determined as a function of r_t.

The NMR relaxometry experiment provides the distribution of the transversal relaxation time $b(T_2)$. The individual relaxation time T_2 is attributed to a pore space with a certain surface to volume ratio A/V by

$$\frac{1}{T_2} = \rho\left(\frac{A}{V}\right), \quad (4)$$

with ρ being the surface relaxivity. Considering that for a capillary tube model with cylindrical pores of radius r, the surface to volume ratio equals $2/r$, we get the following linear relationship between pore radius r and relaxation time T_2 (e.g. Kleinberg, 1996):

$$r = 2\rho T_2 \,. \tag{5}$$

Another approach to derive a pore size distribution is based on the SIP method (Revil et al., 2014, Zhang et al., 2017). Assuming that polarization effects of natural material are caused by different charging and discharging processes of some polarizing cells such as grain surface, pore throat, membrane, and electrical double layer, a decomposition of the polarization effect into several separate relaxation processes can be made. We use the Debye decomposition (Nordsiek and Weller, 2008) to determine the electrical relaxation time distribution as well as the total chargeability from complex conductivity spectra. According to the assumption that the electrical relaxation time and pore size are related to each other, the specific chargeability at a certain relaxation time corresponds to the pore volume attributed to a certain pore size, and the total chargeability is attributed to the total pore volume of the sample. The volume fraction V_c corresponds to the ratio of cumulative chargeability to total chargeability. To transform the relaxation time distribution into a pore size distribution, we adopt the approach proposed by Schwarz (1962) and applied by Revil et al. (2012) for the Stern layer polarization model:

$$r = \sqrt{2\tau D_{(+)}} \,, \tag{6}$$

with $D_{(+)}$ being the diffusion coefficient of the counter-ions in the Stern layer and τ being the relaxation time. Originally, this equation describes the relation between the radius of spherical particles in an electrolyte solution and the resulting relaxation time. Though it remains arguable whether the radius of spherical grains can be simply replaced by the pore radius (Weller et al., 2016), we generally follow this approach. Additionally, we assume a constant diffusion coefficient $D_{(+)} = 3.8\times10^{-12}$ m²/s as proposed by Revil (2013).

The signal amplitude at a given relaxation time corresponds to the pore volume related to the pore radius determined by Eq. (6). Considering the experience that the polarization is related to the specific surface area per unit pore volume (e.g. Weller et al., 2010), we assume that the IP signals are caused by the ion-selected active zones in the narrow pores that are comparable with the pore throats. Their size is quantified by the pore throat radius r_t. Following the procedure proposed by Zhang et al. (2017), the cumulative volume fraction V_c corresponds to the ratio of cumulative chargeability to total chargeability. Considering the restricted range of pore radii (0.1-25 µm) resolved by SIP, a correction of the maximum V_c becomes necessary.

3 Samples and methods

For this study, two different sandstone samples have been used: first, a Bentheimer sandstone, sample BH5-2. The shallow-marine Bentheimer sandstone was deposited during the Early Cretaceous (roughly 140 million years ago) and forms an important reservoir rock for petroleum (Dubelaar et al., 2015). This sandstone is widely used for systematic core analysis due its simple mineralogy and the quite homogeneous and well-connected pore space. It is composed out of 92% quartz, contains some feldspar and about 2.5 vol.-% of kaolinite (Peksa et al., 2015), which is a direct alteration product of the potassium-bearing feldspar minerals. Accordingly, surface area as well as surface relaxivity values are mostly controlled by the kaolinite for this rock.

Secondly, a Röttbacher sandstone, sample RÖ10B, has been used. The Röttbacher sandstone is a fine-grained, more muscovite-illite containing, and rather homogeneous material that was deposited during the Lower Triassic era (roughly 250 million years ago). It is suitable for solid stonework and has been widely used as building material for facades as well as for indoor and outdoor flooring. The Röttbacher sandstone was included in a study on the relationship of pore throat sizes and SIP relaxation times reported by Kruschwitz et al. (2016). This sandstone consists mostly of quartz, but features a higher amount of clay minerals than the Bentheimer sample. Additionally, Fe-bearing minerals (e.g. haematite) have been formed during its arid depositional environment, giving this sandstone a distinct reddish color. Accordingly, surface area as well as surface relaxivity are dominated by the clay and Fe-bearing minerals and should be significantly different than for the BH5-2 sample.

The experimental methods used in this study include digital image analysis based upon micro computed tomography (µ-CT), mercury intrusion porosimetry (MIP), nuclear magnetic resonance (NMR), and spectral induced polarization (SIP).

For this study, a nanotom S 180 X-ray µ-CT equipment (GE sensing and inspection technologies) has been used. The sample size for CT scanning is 2mm diameter and 4mm length. For pore network separation, a combination of manual thresholding and watershed algorithms has been applied to achieve the qualitatively best separated pore space. Additionally, separation results have been cross checked with the images of scanning electrode microscopy (SEM). More details on the digital image analysis workflow can be found in Halisch et al. (2016). The digital image analysis of the 3-D µ-CT data sets provide for each individual pore the volume and the pore radius of the largest sphere that can be placed inside this pore (maximum inscribed sphere method, e.g. Silin and Patzek, 2006). The resulting equivalent pore radius is referred to as pore body radius r_b. Adding up the pore volumes starting with the lowest pore radius yields the cumulative volume fraction of pores V_c (Eq. (1)) as a function of the pore body radius r_b. The µ-CT method can only resolve the part of the pore space with pore sizes larger than the spatial resolution of the 3D image. Considering a voxel size of 1.75 µm of the 3D data set, and a minimum extension of pores of two voxels in one direction, which can be separated by the algorithm, a minimum pore size of 3.5 µm (or minimum pore radius of 1.75 µm) has to be regarded, as for this study, the CT resolution limit is 1.75 µm. Therefore, the pore volume determined by µ-CT does not take into account the pore space with radii smaller than 1.75 µm.

The MIP experiments have been conducted with the PASCAL 140/440 instrument from Thermo Fisher (Mancuso et al., 2012), which covers a pressure range between 0.015 MPa and 400 MPa corresponding to a pore throat radius range from (at best) 1.8 nm to 55 µm. The samples have been evacuated before the MIP experiment. Starting with low pressure, the pores with larger pore throats are filled with mercury. While increasing the pressure, the pores with smaller throats are filled. Reaching a certain pressure level P_c, a cumulative volume of mercury (V_{Hg}) has intruded into the sample that corresponds to the pore volume being accessible by pore throats radii larger or equal r_t according to Eq. (2).

The NMR experiments have been performed with a Magritek Rock Core Analyzer equipment operating at a Larmor frequency of 2 MHz at room temperature (~ 20°C) and ambient pressure. After drying at 105°C for more than 24 hours in vacuum, the samples have been fully saturated with tap water with a conductivity of about 25 mS/m. NMR measurements can be calibrated to get the porosity of the sample. The early time decay signal corresponds to the total water content. The range of resolved pore radii depends on the used value of surface relaxivity. The amplitude b attributed to an individual relaxation time T_2 is related to the volume fraction of pores with the respective pore radius. Considering the larger pores, the resulting radius corresponds to r_b. The smaller pore throats with lower volume yield a lower signal at shorter relaxation times. The cumulative volume fraction of pores V_c is determined by adding up the individual b values starting from the smallest relaxation time and normalizing to the total sum of all b values.

Complex conductivity spectra were recorded using a four-electrode sample holder as described by Schleifer et al. (2002). The spectra were acquired with the impedance spectrometer ZEL-SIP04 (Zimmerman et al., 2008) in a frequency range between 0.002 Hz and 45 kHz at a constant temperature of about 20 °C. Considering that the complex conductivity spectra are affected by electromagnetic coupling effects or other polarization effects at higher frequencies and by a lower signal to noise ratio for lower frequencies, we focus on the frequency range between 0.01 Hz and 100 Hz. The samples were fully saturated with a sodium-chloride solution with a conductivity of 100 mS/m. At least two measurements were performed for each sample to verify the repeatability. The SIP method solely resolves a range of pore radii that depends on the diffusion coefficient. Hence, using $D_{(+)} = 3.8\times10^{-12}$ m²/s in Eq. (6), we get a range of pore radii between 0.1 µm and 10 µm.

4 Results

4.1 Petrophysical properties

Figure 1 (A and C) gives 2-D impressions of the pore system of the Bentheimer sandstone sample. The pore space in general is very well connected, featuring many large and open pores (Fig.1, A & C, blue arrows) and can be described as a classical pore body – pore throat – pore body system. Small pores are mostly found within the clayey agglomerations, which act as (macro) pore filling material (Fig.1, A & C, red arrows) and which are homogeneously distributed throughout the sample material. Figure 1 E gives an impression of the 3-D pore distribution of this sandstone, derived by µ-CT image processing. This favorable structure is directly reflected by the petrophysical properties of this sandstone. The sample investigated in our study is characterized by a porosity of 0.238 measured by MIP, a gas-permeability of 4.25×10^{-13} m² determined by steady-state permeameter (manufactured by Westphal Präzisionstechnik) with a Fancher-type core holder using nitrogen as the flowing fluid, and a specific surface area of 0.3 m²/g determined by Nitrogen adsorption method.

Figure 1 (B and D) shows an impression of the pore space of the Röttbacher sandstone sample from 2-D imaging techniques. Though the (large) pore space is similar structured as it is for the Bentheimer (pore body-throat-body system, Fig. 1, B & D, blue arrows), it is generally reduced (cemented) by clay minerals and features a significantly higher amount of small pores within (Fig. 1, B & D, red arrows). Accordingly, pore space related petrophysical properties classify a more compact rock, which is supported by the 3-D pore distribution, derived by µ-CT image processing (Fig. 1, F). The sample used for this study features a porosity of 0.166 measured by MIP, which is lower than for the Bentheimer sandstone. The gas-permeability is 3.45×10^{-14} m², which is less than 10 % of the value determined for the Bentheimer sandstone. The specific surface area has been measured with 1.98 m²/g and is hence nearly seven times larger than for sample BH5-2, clearly underlining the impact of the clay content. The petrophysical parameters for both samples are compiled in Table 1, whereas results from X-ray fluorescence analysis are summarized in Table 2, regarding the most important chemical components of both sandstones that have been used for this study.

4.2 Pore volume fraction

We applied the methods µ-CT, MIP, NMR, and SIP to get insight into the pore radius distribution of the Bentheimer sandstone sample BH5-2. Figure 2 displays the resolved porosity ϕ_r as a function of pore radius for µ-CT and MIP data. The cumulative pore volume while progressing from larger to smaller pores $V(>r)$ is normalized to the total volume of the sample V_s and results in the resolved porosity

$$\phi_r = \frac{V(>r)}{V_s}, \tag{7}$$

which reaches the true porosity ϕ as threshold value for r approaching zero.

As shown in Figure 2, the µ-CT method identifies the largest pores with pore body radii of about 100 µm. The resolved porosity ϕ_r reaches a value of 0.184 at the limit of resolution of the µ-CT method (r_b=1.75 µm). The nearly horizontal curve progression for r < 17 µm indicates that effectively no significant volume of pores with radii lower than 17 µm were detected or quantified by µ-CT and digital image analysis, respectively. Accordingly, only µ-CT data for r > 17 µm will be taken into account for further analysis.

The MIP identifies the largest pore throats with a radius of about 30 µm. Reaching the limit of resolution of the MIP, the resolved porosity approaches asymptotically the threshold value of 0.238. Though both methods µ-CT and MIP yield the pore radius without any adjustable scaling factor, we observe differences between the two curves $\phi_r(r)$ in Figure 2.

The Röttbacher sample was scanned with resolution 1.5 µm by µ-CT. As shown in Figure 6, the µ-CT method identifies the largest pores with pore body radii of about 90 µm. The resolved porosity ϕ_r reaches a value of 0.106 at the limit of resolution of the µ-CT method (r_b=1.5 µm). As observed for the Bentheimer sandstone, the nearly horizontal curve progression for r < 10 µm indicates that no significant volume of pores with radii lower than 10 µm were detected or quantified by µ-CT and digital image analysis, respectively. Accordingly, only µ-CT data for r > 10 µm will be taken into account for further analysis.

4.3 Pore radius distribution

The description and quantification the pore space in three dimensions requires morphological parameters such as length, width, and thickness of individual pore segments. The parameters are extracted by image analysis software from 3D µ-CT data. We determined the pore length (maximum length of Feret distribution), pore width (minimum width of Feret distribution), and the equivalent diameter of the analyzed pore segment that corresponds to the spherical diameter with equal voxel volume (Schmitt et al., 2016). The minima, maxima, and mean values of the geometrical parameters derived from µ-CT data of the two samples are compiled in Table 3.

The procedures described above result in an individual curve displaying the logarithm of V_c versus the logarithm of the pore radius for each method.

For Bentheimer sandstone, applying the transformation in Eq. (3) for the MIP data and assuming a true porosity of 0.238, the cumulative volume fraction of pores V_c can be displayed as a function of pore radius as shown in Figure 3. The MIP curve gets a fixed position in the plot of Figure 3 without the need for any scaling. It covers a wide range of pore radii between 0.0018 and 44.7 µm.

The curves resulting from other methods have to be adjusted considering the limits of the range of pore radii. The maximum of the µ-CT curve corresponds to V_c = 1 because no larger pore size has been detected by other methods. The maximum resolved porosity of the sample as detected by MIP reaches 0.238. The porosity determined by µ-CT reaches only 0.184 (Figure 2). This value corresponds to a fraction of 0.773

of the porosity determined by MIP. Therefore, the minimum of the µ-CT curve at the pore radius of 17 µm has to be adjusted at $V_c = 1 – 0.773 = 0.227$, because this fraction of pore volume is related to pore radii smaller than 17 µm. The shift of the µ-CT curve to larger pore radii in comparison with MIP is observed in this plot, too.

The T_2 relaxation time distribution of sample BH5-2 is plotted in Figure 4. It indicates a distinct maximum at a relaxation time of 330 ms and two weaker maxima at lower relaxation times. The T_2 relaxation time distribution is transformed into a curve showing the cumulative intensity as a function of T_2. The total intensity is attributed to the total pore volume. The volume fraction V_c corresponds to the ratio of cumulative intensity to total intensity. In order to get the curve V_c as a function of pore radius, the relaxation time T_2 has to be transformed into a pore radius using the surface relaxivity ρ as scaling factor in Eq. (5). Since both µ-CT and NMR method are sensitive to the pore body radius, we expect a similar V_c - r - curve in the overlapping range of pore radii. Assuming a coincidence of the two curves at $V_c = 0.5$, the surface relaxivity is adjusted at $\rho = 54$ µm/s.

Considering the frequency range between 0.01 and 100 Hz and $D_{(+)} = 3.8\times10^{-12}$ m²/s, the relaxation time distribution derived from SIP is attributed to a restricted range of pore radii between 0.1 µm and 10 µm. Assuming that the polarization signals originate from the pore throats, a similarity of pores size distributions resulting from MIP and SIP can be expected. It should be noted that MIP provides the distribution for a wider range of pore radii. Therefore, we adjust the value of V_c at the maximum radius of the SIP to the corresponding value for the MIP curve.

For Röttbacher sandstone, the MIP identifies the largest pore throats with a radius of about 50 µm. Reaching the limit of resolution of MIP, the resolved porosity gets the value of 0.166. Applying the transformation in Eq. (3) on the MIP data and assuming a true porosity of 0.166, the cumulative volume fraction of pores V_c is displayed as a function of pore radius as shown in Figure 7.

We suppose that the MIP method detects the whole pore volume, a porosity of 0.106 recognized by µ-CT corresponds to 63.9% of the total pore volume. Therefore, the minimum of the µ-CT curve at the pore radius of 10 µm has to be adjusted at $V_c = 1 – 0.639 = 0.361$, because this fraction of pore volume is related to pore radii smaller than 10 µm.

The T_2 relaxation time distribution of sample RÖ10B is plotted in Figure 4. It indicates a distinct maximum at a relaxation time of 170 ms. Non-vanishing signals are observed at relaxation times below 0.1 ms. This is an indication of the existence of very small pores in the Röttbacher sandstone.

The position of the NMR curve in the plot of Figure 7 depends on the surface relaxivity ρ. A coincidence with the µ-CT curve at $V_c = 0.5$ requires a surface relaxivity of $\rho = 237$ µm/s for adjusting the NMR curve.

The complex conductivity spectra of the Röttbacher sample are displayed in Figure 5. The processing of the spectra according to the described algorithm results in the V_c - r – curve as shown in Figure 7. The SIP curve is fixed at the value $V_c = 0.9$ that has been determined by MIP for the maximum pore radius resolved by SIP ($r_t = 10$ µm).

5 Discussion

Previous studies have compared the resulting curves (e.g. Zhang and Weller, 2014; Zhang et al., 2017; Ding et al., 2017). The slope of the curves was used to get a fractal dimension. It became obvious that the distribution curves indicate remarkable differences that are caused by the physical principles of the used methods. The methods differ with regard to their limits of resolution. The effective resolution of µ-CT is limited by the voxel size. Larger pores can be easily detected. Nevertheless, even though the derived image (voxel) resolution is quite high (1.75 µm), both sandstone data sets feature no significant volume of pore radii smaller than 10 µm (BH-5) and 17 µm (RÖ-10), respectively. We assume that this is caused by a complex and sensitive mixture of issues about image resolution, image quality (phase contrast), reliability of the watershed-algorithm concerning the separation of individual pores, and hence of the complexity of the pore structure of small pores. The MIP yields the widest range of pore radii. The pore radius is directly related to the pressure. A similarly wide range of pore radii can be resolved by NMR. However, the transformation of the NMR transversal relaxation time into a pore radius requires the surface relaxivity as scaling factor. In a similar way, the transformation of the electrical relaxation time resulting from SIP into a pore radius is based on a scaling factor that depends on the diffusion coefficient. Only a restricted range of pore radii can be resolved by SIP.

Beside the range of pore radii, the geometrical extent of the pore radius differs among the methods. µ-CT enables a geometrical description of the individual pore space considering the shape of the pore. The pore radius can be determined in different ways. We use the average pore radius as an equivalent for the pore body radius r_b. MIP is sensitive to the pore throat radius r_t that enables the access to larger pores behind the throat. The NMR relaxation time is related the pore body radius r_b. We assume that the IP signals are caused by the ion-selected active zones in the narrow pores that are comparable with the pore throats.

Regarding the differences of the methods, we present an approach that combines the curves to get more information on the pore space. Considering the two kinds of pore radii r_b and r_t, we use first µ-CT and NMR to generate a combined curve displaying V_c as a function of r_b. In the next step, we link the curves resulting from MIP and SIP to get a curve showing V_c as a function of the pore throat radius r_t.

It is fundamental that the total pore volume (or total porosity) has to be known. The cumulative pore volume fraction should only consider the pore volume that is resolved in the regarded range of pore radii. Considering the resolution of µ-CT, only the pore space with radii larger than the voxel size is determined. The cumulative pore volume fraction at the limit of resolution has to be adjusted to the non-resolved pore volume. In this way, the µ-CT curve gets a fixed position in the $V_c - r$ plot. Regarding NMR, the relaxation time T_2 has to be transformed into a pore radius according to Eq. (5). The application of Eq. (5) requires the knowledge of the surface relaxivity ρ, which is the necessary scaling factor that causes a shift of the V_c - r curve along the axis of pore radius. Since NMR method is sensitive to the pore body radius, we expect a similar V_c - r curve for NMR and µ-CT in the overlapping range of pore radii. The NMR curve is shifted along the axis of pore radii until a good agreement between the two curves is reached. This procedure enables the adjustment of the surface relaxivity.

MIP is used to generate the curve displaying V_c as a function of r_t over a wide range of pore radii. The SIP curve is fixed at the MIP curve considering the coincidence at the largest pore radius resolved by SIP.

The two curves representing V_c as a function of both r_b and r_t are displayed in a double logarithmic plot. The shift of the two graphs represents the ratio r_b/r_t. Additionally, the slope of the curves is related to the fractal dimension.

The proposed approach in this study results in two pore size distribution curves for the two samples, which are in good accordance to the general pore space structures as described in section 3 and as visualized in Figure 1 (A to F). The first curve combines the distributions resulting from µ-CT and NMR. The µ-CT data provide a pore radius, which is regarded as pore body radius, without any scaling. The scaling of the NMR-curve provides an estimate of the surface relaxivity. The surface relaxivity of the Bentheimer sample reaches 54 µm/s, the corresponding value of the Röttbacher sample is with 237 µm/s much higher. The higher surface relaxivity in comparison with the Bentheimer sample is clearly justified considering the larger specific surface area (Table 1) and the significantly higher content of clay and iron-bearing minerals as indicated in Table 2 (e.g. Keating and Knight, 2010).

The two cumulative pore volume distribution curves for the Röttbacher sample (Figure 7) indicate over the wide range of pore radii a parallel progression with consistently higher values for the pore body radius (µ-CT and NMR) in comparison with the pore throat radius (MIP). The horizontal distance of the two curves yields the ratio r_b/r_t. Regarding the median pore radii at $V_c = 0.5$, a ratio $r_b/r_t = 9.13$ is determined. Considering smaller pores, a ratio $r_b/r_t = 12.15$ is indicated at $V_c = 0.05$.

The parallelism of the pore volume distribution curve is less developed for the Bentheimer sample (Figure 3). We observe a clear distance of the two curves in the range of larger pore radii. Regarding the median pore radii at $V_c = 0.5$, a ratio $r_b/r_t = 2.57$ is determined. For $V_c < 0.2$, the slope of the curves decreases and smaller distances between the curves are observed. The NMR curve in Figure 3 indicates for $V_c > 0.08$ larger pore radii in comparison with the MIP curve and confirms the relationship $r_b > r_t$. The reverse behavior in the interval 0.1 µm < r < 0.6 µm is possibly caused by the low volume fraction (3%) attributed to this range of pore radii. It can be expected that the small amount of water in the small pores causes only weak signals in the NMR relaxometry. Certainly, the resolution of all methods is limited in the range of pore radii that contains only a small volume of water.

Beside the distances between the curves the individual slopes are regarded. The slope (s) of the curve log (V_c) versus log (r) is related to the fractal dimension D of the pore volume ($D = 3 – s$) (Zhang and Weller, 2014). We observe a varying slope in the investigated range of pore radii for the Bentheimer sample. The only range of more or less constant slope, which extends from pore radius 0.1 µm to 10 µm, corresponds to a fractal dimension $D_{MIP} = 2.678$ for MIP, $D_{NMR} = 2.776$ for NMR, and $D_{SIP} = 2.618$ for SIP.

The whole curves of the four methods are non-linear and indicate non-fractal behavior. A Maximum Likelihood Estimator approach (MLE) might be relevant to extract the underlying scaling parameters (Rizzo et al., 2017). For example, in the case of the NMR curve of Bentheimer sandstone, the fitting of all data using the MLE reveals that the log-normal distribution is the most likely distribution with the estimated parameters $\mu = 3.43$ µm and $\sigma = 0.82$ µm. These two scaling parameters are the logarithmic mean and logarithmic standard deviation of the pore radius, respectively. We recognize that the resulting mean radius reaches half value of the effective hydraulic radius ($r_{eff} = 6.97$ µm).

We observe a constant slope of the NMR curve for the Röttbacher sample (Figure 7) in the interval 0.01 µm < r_b < 100 µm. A similar slope is observed for the MIP curve in the interval 0.01 µm < r_t < 10 µm. Considering the overlapping pore throat radii range between 0.1 µm and 10 µm, a fractal dimension D with values of 2.640 for MIP, and 2.661 for NMR has been determined. The slightly higher slope of the SIP curve results in a lower value of fractal dimension ($D = 2.533$).

Our approach enables the integration of SIP in the determination of a pore throat size distribution. Considering the limited frequency range, only a limited range of pore throat radii can be reflected. Using a fixed diffusion coefficient $D_{(+)} = 3.8\times10^{-12}$ m²/s, a range of pore throat radii between 0.1 µm and 10 µm is resolved. The SIP curve is linked to the MIP curve at $r = 10$ µm. The proposed procedure results in a fair agreement between SIP and MIP curves in the overlapping range of pore throat radius for both the Bentheimer and the Röttbacher sample. In comparison with MIP, a slight overestimation of V_c is observed for larger pore throat radii and a underestimation for lower pore throat radii. Considering the two samples of the presented study, the assumption of a constant diffusion coefficient seems to be justified. Regarding the discussion on the most relevant parameter that controls the relaxation time, our assumption that the pore throat radius is related to the relaxation time is supported by the results.

6 Conclusions

Pore radii distributions have been determined by different methods (µ-CT, MIP, NMR, and SIP) for two sandstone samples. The curves presenting the cumulative distribution of pore volume V_c as a function of pore size have proved to be a suitable tool for comparison. It becomes obvious that the distribution curves indicate remarkable differences that are based on the physical principles of the used methods. The methods differ with regard to their limits of resolution. The effective resolution of µ-CT is limited by the voxel size

(1.75 µm). Larger pores can be easily detected, whereas quantification of small pores and volumes of pores with small radii is severely affected by the image quality and the image processing algorithms. The MIP yields the widest range of pore radii. The pore radii are directly related to the pressure interval. A similar wide range of pore radii can be achieved by NMR. However, the transformation of the NMR transversal relaxation time into a pore radius requires the surface relaxivity as scaling factor. In a similar way, the transformation of the electrical relaxation time resulting from SIP into a pore radius is based on a scaling factor that depends on the diffusion coefficient. Only a restricted range of pore radii (0.1 µm to 10 µm) can be resolved by SIP.

Beside the range of pore radii, the geometrical extent of the pore radius differs among the methods. µ-CT enables a geometrical description of the individual pore space considering the shape of the pore. The pore radius can be determined in different ways. We use the average pore radius as an equivalent for the pore body radius r_b. MIP is sensitive to the pore throat radius r_t that enables the access to larger pores behind the throat. The NMR relaxation time is related to an average pore body radius r_b. We assume that the IP signals are caused by the ion-selected active zones in the narrow pores that are comparable with the pore throats.

Considering the two kinds of pore radii r_b and r_t, we use µ-CT and NMR to generate a combined curve displaying V_c as a function of r_b. A good agreement between the two curves is achieved if they coincide at $V_c = 0.5$. This condition is used to determine the surface relaxivity, which is in good accordance to the investigated surface area and mineralogy of the sample materials. MIP is used to generate the curve displaying V_c as a function of r_t over a wide range of pore radii. The SIP curve is fixed at the MIP curve considering the coincidence at the largest pore radius resulting from SIP.

The two curves representing V_c as a function of both r_b and r_t are displayed in a double logarithmic plot. The shift of the two graphs represents the ratio r_b/r_t. Additionally, the slope of the curves is related to the fractal dimension.

The investigations on the samples demonstrate that the porosity increases using a method with a higher resolution. Both porosity and pore volume are parameters that depend on the resolution. The fractal dimension describes the size of geometric objects as a function of resolution. Therefore, the knowledge of fractal behavior enables upscaling and downscaling of geometric quantities. The Bentheimer sandstone sample is characterized by a ratio $r_b/r_t = 2.57$ for the larger pores. A fractal behavior is observed in the range of pore radii between 0.1 µm and 10 µm with an average $D = 2.69$ determined for the pore volume by MIP, NMR, and SIP. The Röttbacher sandstone sample indicates with $r_b/r_t = 9.13$ a larger ratio between pore body radius and pore throat in comparison with the Bentheimer sample. An average fractal dimension of $D = 2.61$ is determined for the Röttbacher sample.

Acknowledgements

The authors thank Sven Nordsiek (University Bayreuth) for the Debye decomposition of the SIP data, Dietmar Meinel (BAM, Berlin) for supporting the CT analysis, Carsten Prinz (BAM, Berlin) for providing the MIP data, and Mike Müller-Petke as well as Raphael Dlugosch (both LIAG) for the acquisition of the NMR spectra for this study. Dr. Zeyu Zhang thanks Bundesanstalt für Materialforschung und –prüfung (BAM, Berlin) for the Adolf-Martens-Fellowship that enabled his stay in Germany for the experimental research.

References

Avnir, D., and Jaroniec, M.: An isotherm equation for adsorption on fractal surfaces of heterogeneous porous materials, Langmuir, 5, 6, 1412–1433, 1989.

Avnir, D., Farin, D., and Pfeifer, P.: Molecular fractal surfaces, Nature, 308, 261-263, 1984.

Behroozmand, A., Keating, K., and Auken, E.: A review of the principles and applications of the NMR technique for near-surface characterization, Surv Geophys, 36, 27–85, doi: 10.1007/s10712-014-9304-0, 2015.

Ding, Y., Weller, A., Zhang, Z., and Kassab, M.: Fractal dimension of pore space in carbonate samples from Tushka Area (Egypt), Arabian Journal of Geosciences, 10, 388, doi: 10.1007/s12517-017-3173-z, 2017.

Dubelaar, W. C., and Nijland, T. G.: The Bentheim Sandstone: geology, petrophysics, varieties and its use as dimension stone, in: Engineering Geology for Society and Territory, 8, Lollino, G., Giordan, D., Marunteanu, C., Christaras, B., Yoshinori, I., and Margottini, C. (Eds.), Springer International Publishing, Switzerland, 557-563, 2015.

Gaboreau, S., Robinet, J. C., Tournassat, C., and Savoye, S.: Diffuse transport in clay media: µm to nm scale characterization of pore space and mineral spatial organization: International Meeting Clays in Natural and Engineered Barriers for Radioactive Waste Confinement, Montpellier, France, October 2012, hal-00705345, 2012.

Halisch, M., Schmitt, M., and Fernandes, C. P.: Pore Shapes and Pore Geometry of Reservoirs Rocks from µ-CT Imaging and Digital Image Analysis, in: Proceedings of the Annual Symposium of the SCA 2016, Snowmass, Colorado, USA, 21-26 August 2016, SCA2016-093, 2016.

Halisch, M., Steeb, H., Henkel, S., and Krawczyk, C. M.: Pore-Scale tomography and imaging: applications, techniques and recommended practice, Solid Earth Special Issue, Solid Earth, 7, 1141-1143, doi:10.5194/se-7-1-2016, 2016.

Keating, K., and Knight, R.: A laboratory study of the effect of Fe(II)-bearing minerals on nuclear magnetic resonance (NMR) relaxation measurements, Geophysics, 75, 3, F71–F82, 2010.

Keller, L. M., Holzer, L., Wepf, R., Gasser, P., Münch, B., and Marschall, P.: On the application of focused ion beam nanotomography in characterizing the 3D pore space geometry of Opalinus clay, Physics and Chemistry of the Earth, 36, 1539-1544, doi:10.1016/j.pce.2011.07.010, 2011.

Kelokaski, M., Siitari-Kauppi, M., Sardini, P., Mori, A., and Hellmuth, K.H.: Characterisation of pore space geometry by ^{14}C-PMMA impregnation-development work for in situ studies, Journal of Geochemical Exploration, 90, 45-52, doi:10.1016/j.gexplo.2005.09.005, 2005.

Kleinberg, R. L.: Utility of NMR T_2 distributions, connection with capillary pressure, clay effect, and determination of the surface relaxivity parameter ρ2, Magnetic Resonance Imaging, 14, 761–767, 1996.

Kruschwitz, S., Prinz C., and Zimathies A.: Study into the correlation of dominant pore throat size and SIP relaxation frequency, Journal of Applied Geophysics, 135, 375-386, 2016.

Mandelbrot, B. B.: Fractals: form, chance, and dimension, Freeman, San Francisco, 1977.

Mandelbrot, B. B.: Fractal geometry of nature, Freeman, San Francisco, 1983.

Mancuso, C., Jommi, C., and D'Onza, F. (Eds.): Unsaturated Soils: Research and Applications, Volume 1, Springer-Verlag Berlin Heidelberg, 123-130, doi: 10.1007/978-3-642-31116-1, ISBN: 978-3-642-31115-4 (Print), 2012.

Mees, F., Swennen, R., van Geet, M., and Jacobs, P. (Eds.): Applications of X-ray computed tomography in the geosciences, Geological Society, London, Special Publication, 215, 1, 1-6, doi: 10.1144/GSL.SP.2003.215.01.01, 2003.

Meyer, K., Klobes, P., and Röhl-Kuhn, B.: Certification of reference material with special emphasis on porous solids, Crystal Research and Technol., 32, 173-183, 1997.

Nordsiek, S., and Weller, A.: A new approach to fitting induced-polarization spectra, Geophysics, 73, 6, F235-F245, doi: 10.1190/1.2987412, 2008.

Pape, H., Riepe, L., and Schopper, J. R.: A pigeon-hole model for relating permeability to specific surface, The Log Analyst, 23, 1, 5–13, 1982.

Pape, H., Arnold J., Pechnig R., Clauser C., Talnishnikh E., Anferova S., and Blümlich B.: Permeability prediction for low porosity rocks by mobile NMR, Pure and Applied Geophysics, 166, 1125-1163, 2009.

Peksa, A., Wolf, K., and Zitha, P.: Bentheimer sandstone revisited for experimental purposes, Marine and Petroleum Geology, 67, 701-719, doi: 10.1016/j.marpetgeo.2015.06.001, 2015.

Peth, S., Horn, R., Beckmann, F., Donath, T., Fischer, J., and Smucker, A. J. M.: Three-dimensional quantification of intra-aggregate pore-space features using Synchrotron-Radiation-Based Microtomography, Soil Science Society of America journal, 72, 4, 897-907, doi: 10.2136/sssaj2007.0130, 2008.

Revil, A., Koch, K., and Holliger, K.: Is it the grain size or the characteristic pore size that controls the induced polarization relaxation time of clean sands and sandstones?, Water Resources Research, 48, W05602, doi: 10.1029/2011WR011561, 2012.

Revil, A.: Effective conductivity and permittivity of unsaturated porous materials in the frequency range 1 mHz-1GHz, Water Resources Research, 49, 306-327, doi: 10.1029/2012WR012700, 2013.

Revil, A., Florsch, N., and Camerlynck, C.: Spectral induced polarization porosimetry, Geophysical Journal International, 198, 1016-1033, doi: 10.1093/gji/ggu180, 2014.

Rizzo, R.E., Healy, D., and De Siena, L.: Benefits of maximum likelihood estimators for fracture attribute analysis: Implications for permeability and up-scaling, Journal of Structural Geology, 95, 17-31, doi: 10.1016/j.jsg.2016.12.005, 2017.

Rouquerol, J., Avnir, D., Fairbridge, D. C. W., Everett, D. H., Haynes, J. H., Pernicone, N., Ramsay, J. D. F., Sing, K. S. W., and Unger, K. K.: Recommendations for the characterization of porous solids (Technical Report), Pure and Appl. Chem., 66, 1739-1758, 1994.

Schleifer, N., Weller, A., Schneider, S., and Junge, A.: Investigation of a Bronze Age plankway by spectral induced polarization, Archeological Prospection, 9, 243–253, doi: 10.1002/arp.194, 2002.

Schmitt, M., Halisch, M., Müller, C., and Fernandes, C. P.: Classification and quantification of pore shapes in sandstone reservoir rocks with 3-D X-ray micro-computed tomography, Solid Earth, 7, 285–300, doi:10.5194/se-7-285-2016, 2016.

Schwarz, G.: A theory of the low-frequency dielectric dispersion of colloidal particles in electrolyte solution, Journal of Physical Chemistry, 66, 2636-2642, doi: 10.1021/j100818a067, 1962.

Silin, D. and Patzek, T.: Pore space morphology analysis using maximal inscribed spheres, Physica A, 371, 2,336-360, doi: 10.1016/j.physa.2006.04.048, 2006.

Thomeer, J. H. M.: Introduction of a pore geometrical factor defined by the capillary pressure curve, Journal of Petroleum Technology, 12(3), 73-77, 1960.

Washburn, E. W.: The dynamics of capillary flow, Physical Review, 17, 3, 273-283, 1921.

Weller, A., Zhang, Z., Slater, L., Kruschwitz, S., and Halisch, M.: Induced polarization and pore radius – a discussion, Geophysics, 81, 5, D519-526, doi:10.1190/GEO2016-0135.1, 2016.

Weller, A., Slater, L., Binley, A., Nordsiek, S., and Xu, S.: Permeability prediction based on induced polarization: Insights from measurements on sandstone and unconsolidated samples spanning a wide permeability range, Geophysics, 80, 2, D161-D173, doi:10.1190/GEO2014-0368.1, 2015.

Weller, A., Nordsiek, S., and Debschütz, W.: Estimating permeability of sandstone samples by nuclear magnetic resonance and spectral-induced polarization, Geophysics, 75, E215 – E226, doi: 10.1190/1.3507304, 2010.

Zhang, Z., Weller, A., and Kruschwitz, S.: Pore radius distribution and fractal dimension derived from spectral induced polarization, Near Surface Geophysics, 15, 625-632, doi: 10.3997/1873-0604.2017035, 2017.

Zhang, Z., and Weller, A.: Fractal dimension of pore space geometry of an Eocene sandstone formation, Geophysics, 79, D377-387, doi:10.1190/GEO2014-0143.1, 2014.

Zimmermann, E., Kemna, A., Berwix, J., Glaas, W., and Vereecken., H.: EIT measurement system with high phase accuracy for the imaging of spectral induced polarization properties of soils and sediments, Measurement Science and Technology, 19, 9, 094010, doi: 10.1088/0957-0233/19/9/094010, 2008.

Table 1: Petrophysical properties of the samples: porosity ϕ, permeability K, specific surface area S_m, formation factor F, dominant pore radius r_{dom}, effective pore radius r_{eff}, the ratio r_b / r_t, fractal dimensions determined from mercury intrusion porosimetry D_{MIP}, nuclear magnetic resonance D_{NMR}, and spectral induced polarization D_{SIP}, the surface relaxivity ρ, and the Diffusion coefficient $D_{(+)}$.

	unit	BH5-2	RÖ10B
Porosity (triple weighing)		0.238	0.159
Porosity (µ-CT)		0.184	0.106
Porosity (MIP)		0.238	0.166
Permeability K	m²	4.25×10^{-13}	3.45×10^{-14}
Specific surface area	m²/g	0.30	1.98
Formation factor F		14.3	11.3
r_{dom} (MIP)	µm	11.4	4.9
$r_{eff} = (8FK)^{0.5}$	µm	6.97	1.77
r_b / r_t		2.57	9.13
D_{MIP}		2.678	2.640
D_{NMR}		2.776	2.661
D_{SIP}		2.618	2.533
Surface relaxivity ρ	µm/s	54	237
Diffusion coefficient $D_{(+)}$	m²/s	3.8×10^{-12}	3.8×10^{-12}

Table 2: Chemical components of the samples from X-ray Fluorescence analysis.

	Selected chemical components from X-Ray Fluorescence [weight-%]						
Sample	SiO_2	TiO_2	Al_2O_3	Fe_2O_3	CaO	Na_2O	K_2O
BH5-2	97.84	0.048	1.2	0.05	0.019	0.02	0.355
RÖ10B	87.06	0.356	6.06	1.07	0.225	0.13	3 679

Table 3: Geometrical parameters of individual pores derived from µ-CT data of the two samples.

descriptor	Sample					
	BH5-2			RÖ10B		
	min. [µm]	max. [µm]	mean [µm]	min. [µm]	max. [µm]	mean[µm]
equivalent pore diameter	2.17	229.1	71.56	1.86	230.4	28.95
Feret length (length 3D)	1.92	537.1	161.8	1.64	416.8	56.3
Feret Width (width 3D)	1.92	307.0	87.45	1.64	265.8	28.28
Feret breadth (breadth 3D)	1.75	379.4	114.7	1.5	354.8	37.99
pore volume	5.36	6294270	315069	3.38	6404830	64809

[µm³]							

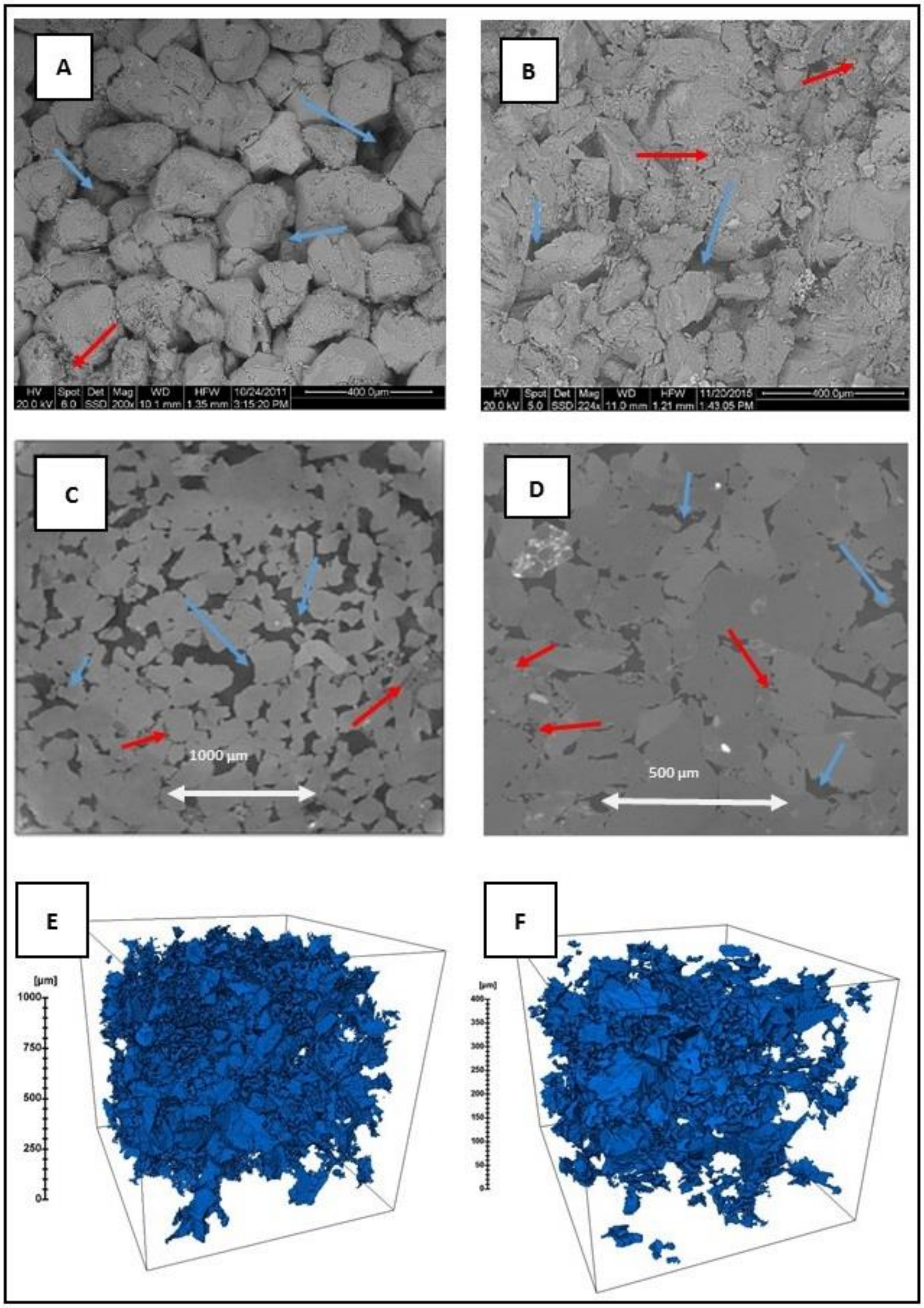
A
HV 20.0 kV
Spot 6.0
Det SSD
Mag 200x
WD 10.1 mm
HFW 1.35 mm
10/24/2011 3:15:20 PM
400.0µm
B
HV 20.0 kV
Spot 5.0
Det SSD
Mag 224x
WD 11.0 mm
HFW 1.21 mm
11/20/2015 1:43:05 PM
400.0µm
C
1000 µm
D
500 µm
E
[µm]
1000
750
500
250
0
F
[µm]
400
350
300
250
200
150
100
50
0

Figure 1: SEM (A) and 2D (C) and 3D (E) CT views upon the minerals and pore structure of the investigated sample of Bentheimer sandstone, and SEM (B) and 2D (D) and 3D (F) CT views upon the minerals and pore structure of the investigated sample of Röttbacher sandstone. Blue arrows indicate open pore spaces, red arrows indicate clay agglomerations and pore fillings.

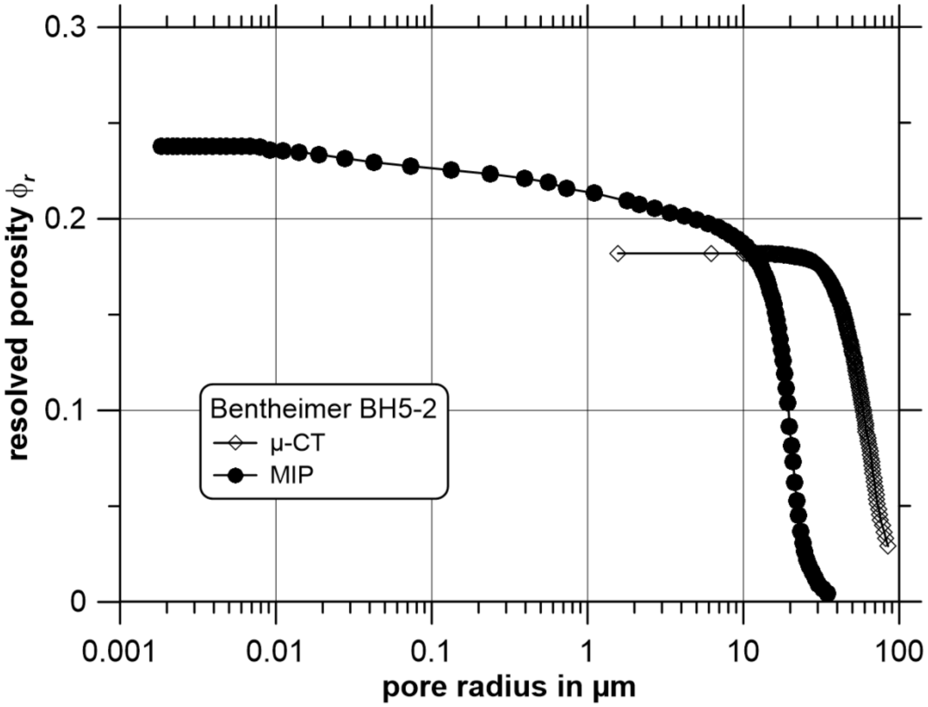

Figure 2: The recognized porosity and pore size range of Bentheimer sandstone sample BH5-2. The maximum porosity recognized by MIP is 0.238 and the maximum porosity recognized by µ-CT is 0.184.

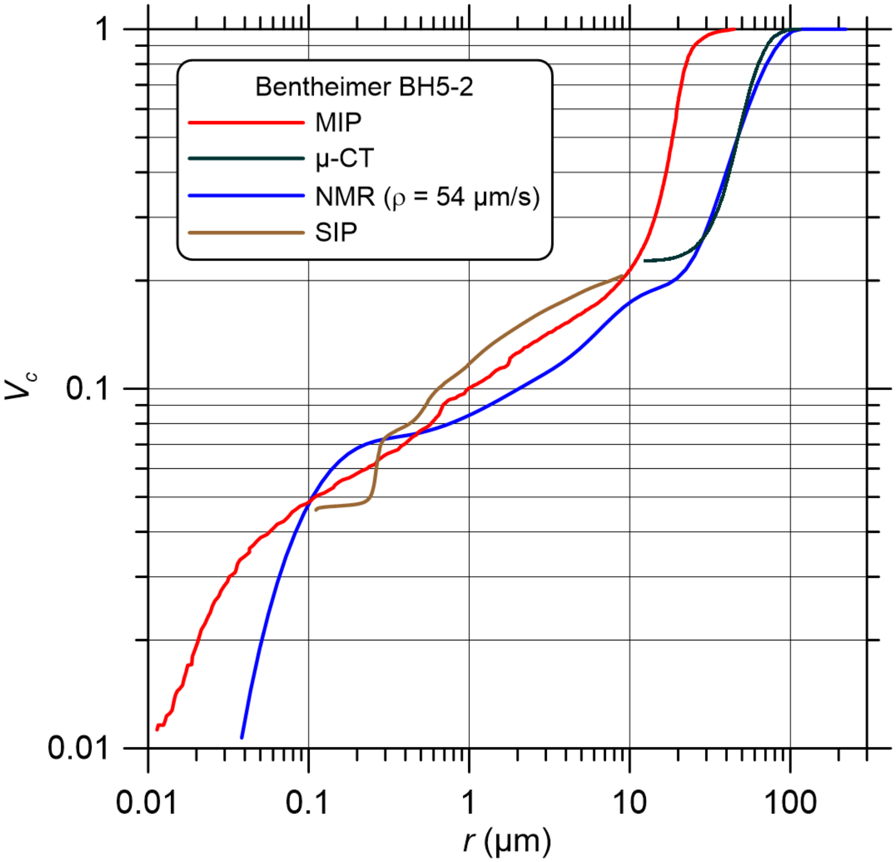

Figure 3: The comparison of V_c-r curves determined from MIP, µ-CT, NMR and SIP for Bentheimer sandstone sample BH5-2.

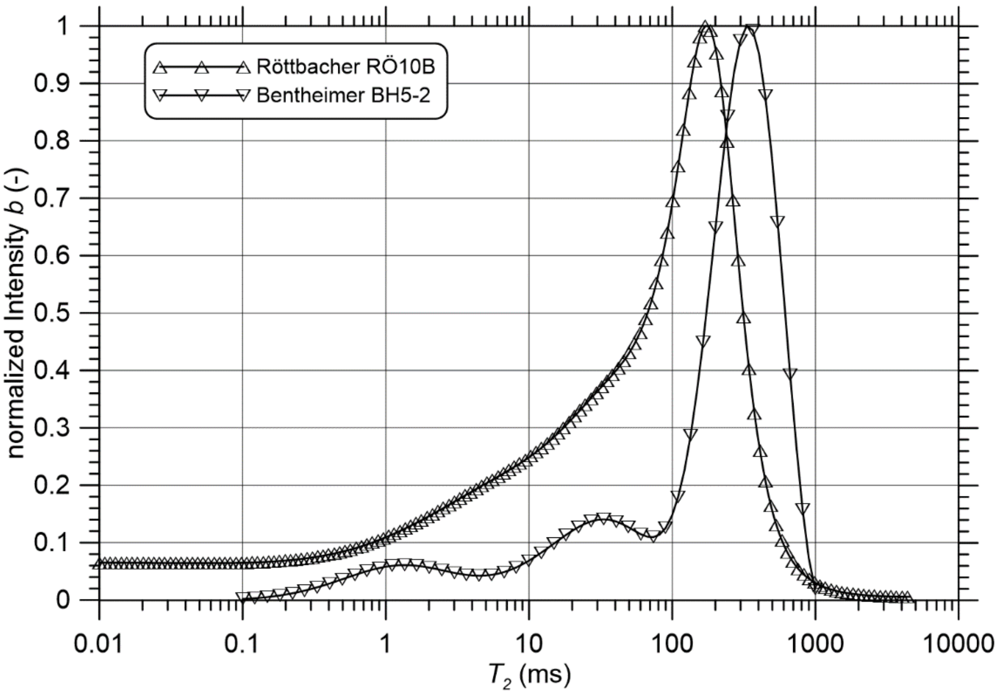

Figure 4: The NMR T_2 relaxation time distributions of samples BH5-2 and RÖ10B.

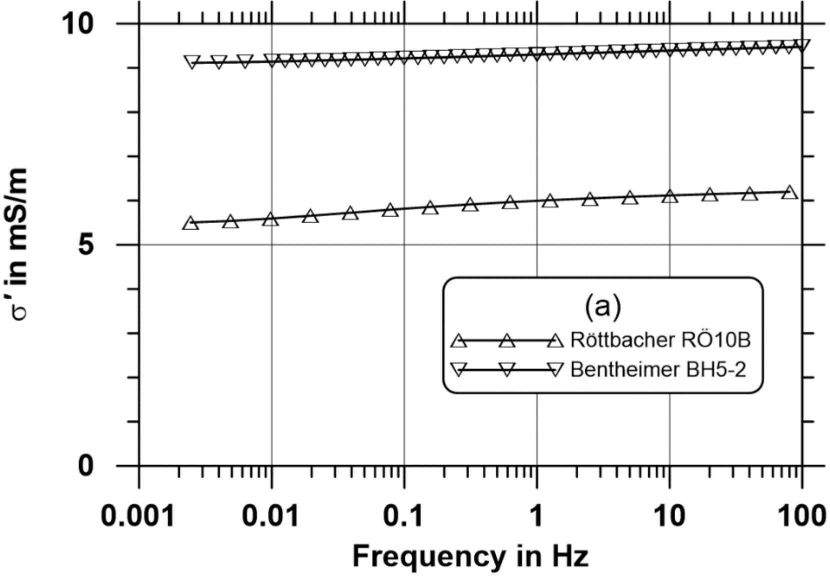

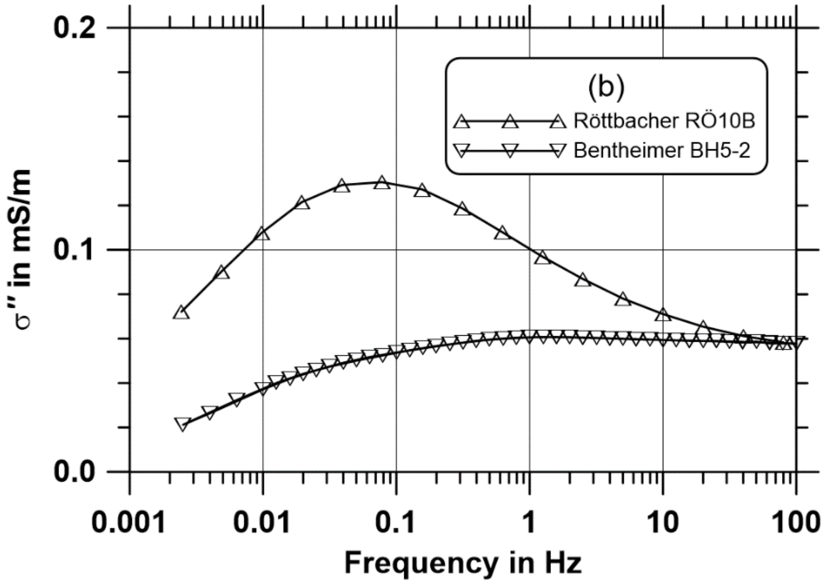

Figure 5: Measured complex conductivity spectra of samples BH5-2 and RÖ10B. a) real part of conductivity, b) imaginary part of conductivity.

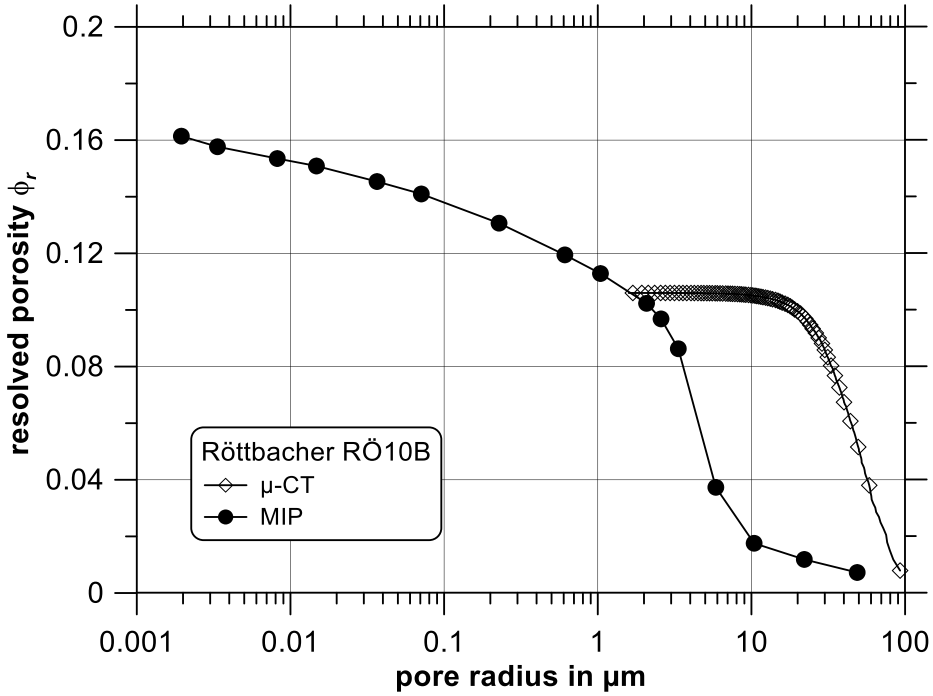

Figure 6: The recognized porosity and pore size range of Röttbacher sandstone sample RÖ10B. The maximum porosity recognized by MIP is 0.166 and the maximum porosity recognized by μ-CT is 0.106.

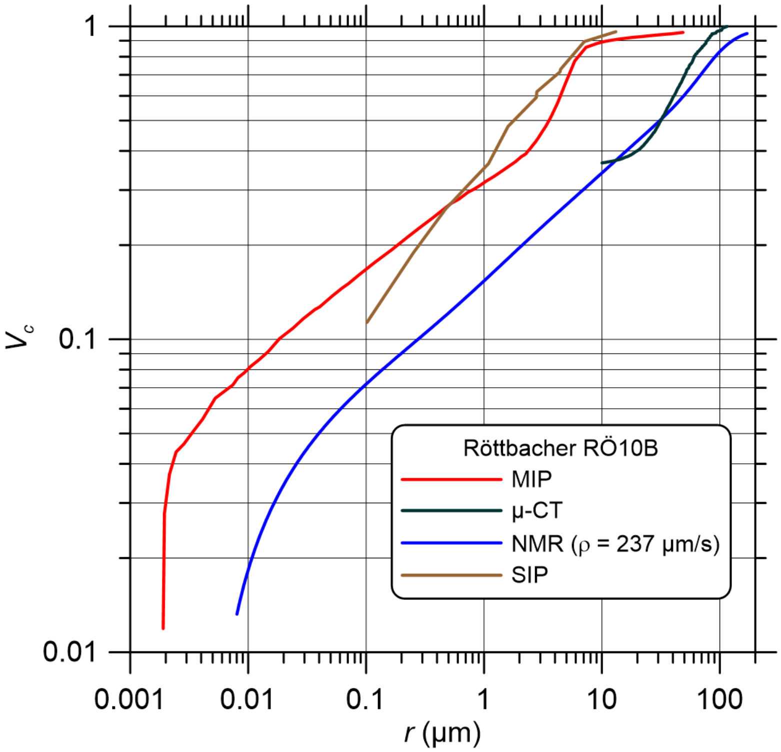

Figure 7: The comparison of V_c-r curves determined from MIP, μ-CT, NMR and SIP for Röttbacher sandstone sample RÖ10B.